



# Investigation of Hardness, Microstructure, and Process Temperature in the Internal Gear Flow-Forming Process

M. Khodadadi<sup>1</sup> · K. Khalili<sup>1</sup> · A. Ashrafi<sup>1</sup> · F. Kolahan<sup>2</sup>

Received: 21 March 2022 / Accepted: 2 November 2022  
© The Society for Experimental Mechanics, Inc 2023

## Abstract

The advantages of the flow-forming process, such as excellent mechanical properties, simple tools, and the need for low forming force, have led to the increasing use of this process in various industries, especially in the military, aerospace, and automotive industries. New application of this process is the internal gear flow-forming process (IGFP), in which the gear is produced with simple tools and low forming force. In this paper, IGFP was studied by the finite element method and experiments. Experiments include tensile test (determine stress-strain curve of the material), ring compression test (determine friction coefficient), flow-forming test, and metallography. The material was considered elastic-plastic, and the Coulomb friction model was used to simulate the friction between surfaces. IGFP was performed by a simple setup. Teeth height and gear profile were measured and compared to simulated values, and there is a good agreement between the simulation and experimental results. Once the simulation is verified, the effects of process parameters (feed rate, roller diameter, attack angle of the roller, and thickness reduction percentage) on the process temperature were obtained using the design of experiments (DOE). According to DOE results, thickness reduction percentage (T) and roller diameter (D) have the most significant effect on process temperature. Finally, a function for process temperature was obtained versus input parameters, and this function was optimized by the firefly algorithm.

**Keywords** Flow-forming · Internal gear · Optimization · Firefly algorithm · Finite element simulation

## Introduction

Flow-forming is a progressive, eco-friendly, chipless metal forming method that uses a rotary point deformation approach [1, 2]. In this process, the mandrel is installed on the main spindle of the machine, and a tube is mounted on the mandrel. By moving one or more rollers on the pre-form and inducing continuous and localized plastic deformation on the tube, the material is displaced axially [3, 4]. The advantages of the flow-forming process, such as excellent mechanical properties, simple tools, and the need for low forming force, have led to its increasing use in various industries, especially in the military, aerospace, and automotive industries [3, 5–10]. Depending on the geometry of

the mandrel, cylinders, cones, or tubes with internal teeth can be produced. The internal gear flow-forming process (IGFP) is a new application of this process for manufacturing internal gears [11–14]. Gears are generally manufactured by chipping operations. To overcome cutting problems (long machining time, material waste, and poor mechanical properties), flow-forming can be used for manufacturing internal gears [15, 16].

Flow-formed tubes with internal teeth have been investigated by some researchers using experiments and theoretical analysis. Groche and Fritsche [11] concluded that in the production of internal gears by the flow-forming process, the number of rollers affects mandrel erosion. The influences of thickness reduction, roller diameter, and feed rate on the tube microstructure, surface roughness, and teeth height were investigated by Jiang et al. [17–20] in the ball spinning of thin-wall tubes with internal ribs. Flow-forming of splines was studied by Haghshenas et al. [21–23]. They investigated the effects of strain hardening rate, hardness, microstructure, and thickness reduction percentage on the plastic strain in FCC metals. Analyzing trapezoidal internal gear production

✉ K. Khalili  
kkhalili@birjand.ac.ir

<sup>1</sup> Department of Mechanical Engineering, University of Birjand, Birjand, Iran

<sup>2</sup> Department of Mechanical Engineering, Ferdowsi University of Mashhad, Mashhad, Iran



**Table 1** Chemical composition of C12200

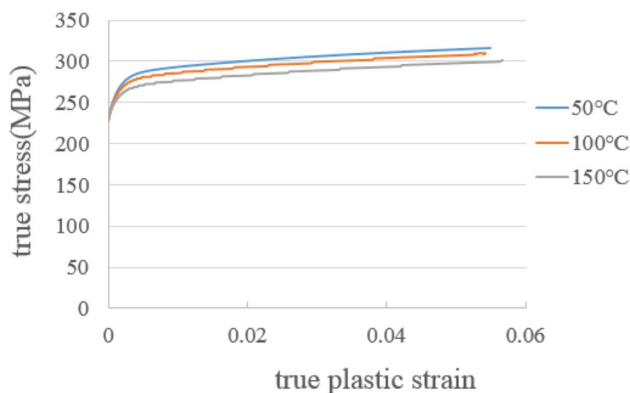
Zn	Pb	Fe	Ni	AL	Si	Mn	Sb	Cu
0.029	0.006	0.033	0.012	0.030	0.007	0.003	0.004	99.877

defects was done by Xia et al. [24, 25] experimentally and numerically. The multi-step spinning of internal gear using a plate blank was investigated by Xu et al. [26], both numerically and experimentally. Khodadadi et al. [12–14] studied the IGFP experimentally and numerically and then explored the influence of input parameters on tooth height, process force, and built-up edge.

According to the literature review, IGFP is a new process that needs further investigation. IGFP has a more sophisticated deformation process than equivalents without inner ribs. The effect of parameters on process force, teeth height, and built-up edge has been studied in previous research [12–14]. In the present study, the effect of parameters on process temperature is investigated, and then it is optimized. The process parameters should be selected so that the temperature is minimized. Meta-heuristic algorithms are usually used in combination with the design of experiments (DOE), in which only small-scale experiments are necessary to represent the whole experimental region in this case [27]. The response surface method (RSM) was used to obtain the objective function, and then the meta-heuristic algorithm (Firefly) was used to optimize this function.

## Materials and Method

In this research, several experiments have been performed. First, a simple tensile test was performed to obtain the stress-strain curve of the preform. Then, a ring compression test was performed to get the coefficient of friction between the roller-preform and the preform-mandrel. The flow-forming process

**Fig. 1** True stress-true plastic strain diagram of the preform at various temperatures

was performed on the workpiece, and at the end, the microstructure and hardness of the workpiece were examined.

The preform used is a copper tube with a thickness of 2.5 mm, an inner diameter of 13.2 mm, and a length of 30 mm. The material of the preform was C12200 copper alloy. Chemical analysis was performed, and the results are shown in Table 1. The mandrel is a gear with 20 teeth, a 13.2 mm outer diameter, and a modulus of 0.6 mm, which was cut on a rod made of CK45 steel. Then the surface hardening heat treatment is performed on it so that its surface does not suffer from wear and corrosion. A roller bearing (SKF 6203/VA201) with a width of 12 mm and a diameter of 40 mm was used as a roller, which, in addition to the rotation without friction, also has high strength and stiffness.

During the flow-forming process, due to the friction between the tools and the workpiece, the temperature increases, and this increase in temperature affects the mechanical properties. Therefore, the plastic behavior and the material's properties at high temperatures must also be determined. The ASTM-E8 standard was used to prepare the test samples. The tests were carried out at temperatures of 50, 100, and 150 degrees Celsius at a rate of 20 mm/min. True stress ( $\sigma$ ) and strain ( $\epsilon$ ) are obtained from equation (1) (up to the necking point):

$$\sigma = S(1 + e), \quad \epsilon = \ln(1 + e) \quad (1)$$

$S$  : engineering stress,  $e$  : engineering strain

After the necking point, true strain and stress can be obtained from equation (2), and usually, after the necking point, the relationship between stress and strain is assumed to be linear [28].

$$\sigma = \frac{F}{A} \quad \sigma_f = \frac{F}{A_f} \quad (2)$$

$$\epsilon = \ln \frac{L}{L_0} \quad \epsilon_f = \ln \frac{L_f}{L_0} = Ln \frac{A_0}{A_f}$$

The stress-strain curve and the mechanical properties of C12200 are shown in Fig. 1 and Table 2. Friction has a significant role in metal forming processes and must be considered during the process. The flow pattern of materials and defects created in the products is strictly controlled by frictional conditions. Choosing the appropriate friction

**Table 2** Mechanical properties of C12200

material	$\sigma_y$ (MPa)	$\sigma_u$ (MPa)	E(GPa)	$\nu$	$\rho$ (kg/m <sup>3</sup> )
C12200	227	295	115	0.3	8930

coefficient and the proper test method is essential to understanding the friction phenomenon between the contact surface of the part and the mold. Among all the methods of measuring the friction coefficient, the ring compression test is the most commonly used [29–32]. Because the temperature increases during the flow forming process and temperature changes also affect the friction coefficient, the ring compression test was performed at 30, 60, 90, and 130°C. Rings having a typical geometrical ratio of 2:3:6 were used as test samples (thickness of 8 mm, internal diameter of 12 mm, and external diameter of 24 mm). Figure 2 presents the ring compression sample, and the setup of the ring compression test is shown in Fig. 3. Calibration curves must be obtained to find the friction coefficient (friction factor) in the forming processes. Although the more accurate friction coefficient, the more accurate simulation results of the process can be achieved, as the main focus of the current study is to simulate the flow-forming process, we did not obtain the calibration curve. The friction coefficient is obtained as follows at different temperatures:

The friction coefficient was calculated by finite element analysis software after doing the ring compression test on copper workpieces and measuring their final dimensions. In this way, after simulating the process, different values are defined as the friction coefficient for simulation. For each of these coefficients, the inner and outer diameter of the ring is obtained for the compressed ring. Finally, after

comparing these dimensions with the dimensions of the compressed ring obtained from the experiment, the friction coefficients at different temperatures were estimated. The friction coefficient at different temperatures is according to Table 3. The stress-strain curve of the preform and friction coefficient were determined using a Zwick/Roel tensile test equipment with a maximum load of 650 kN and servo motor control.

In this study, the flow-forming process was done on a universal lathe machine. The preform was created by machining copper rods. After preparing the preform and cleaning its inner surface, the outer surface of the mandrel and the tube's inner surface were impregnated with oil, so that after the process, the product could be easily removed from the mandrel. Dip the mandrel surface in oil and then mount the preform on it. The mandrel is then inserted into the spindle, and both begin to rotate at a speed of 500 rpm, simultaneously. The feed rate of the roller is 0.11 mm/rev. The experimental setup is shown in Fig. 4. The minimum thickness reduction, usually 15%, is determined to ensure that the plastic metal flow is not restricted to the exterior surface [33]. The preform and flow-formed gear are shown in Fig. 5. The profile and tooth height of the gear were measured using a video measuring machine (VMM).

Fig. 2 Dimensions of the ring compression test sample

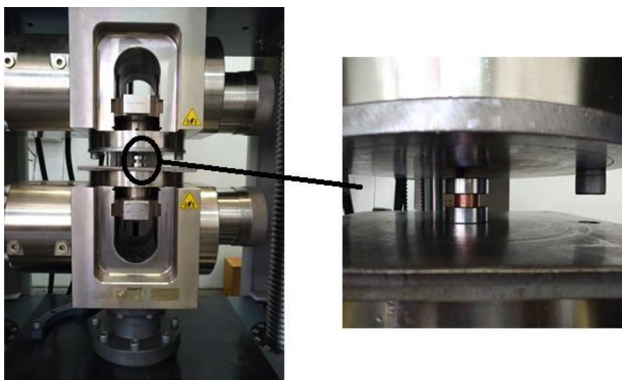
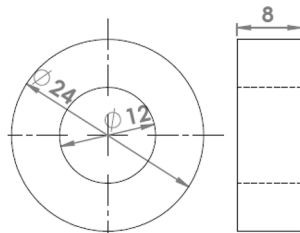


Fig. 3 Setup of the ring compression test

Table 3 Friction coefficients obtained at different temperatures

temperature(°C)	30	60	90	130
Friction coefficient	0.05	0.07	0.1	0.13

Fig. 4 Experimental setup of the flow-forming process (assembled mandrel and preform)

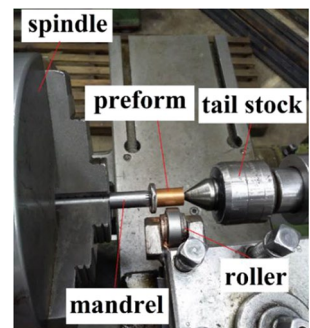
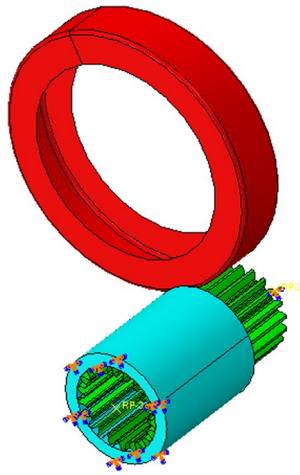


Fig. 5 Used preform in flow-forming and flow-formed gear



**Fig. 6** Schematic of backward flow-forming in FEM model



## Simulation of Flow-Forming Process

In this analysis, three parts were used, including preform, roller, and mandrel, whose geometrical dimensions were

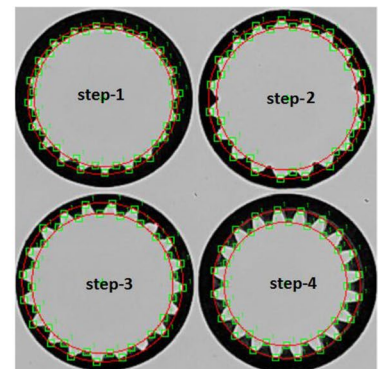
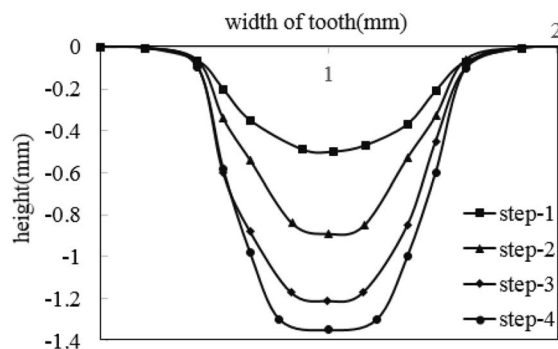
**Table 4** Flow-forming parameters in simulation

Thickness reduction (%)	25, 44, 55, 62
Roller diameter (mm)	40
Mandrel diameter (mm)	13.2
Feed rate (mm/rev)	0.11
Spindle rotation (rpm)	500



**Fig. 7** The final product of IGFP

**Fig. 8** Tooth height and form of internal gear in the experiment



given in section 2. The preform was considered an elastic-plastic deformable part and meshed by 41470 elements of the C3D8RT type. The plastic behavior of the preform was defined in the software as a point-by-point stress-strain curve. The roller and mandrel were considered rigid bodies. Figure 6 shows the assembled set of components in the simulation software. A thermo-mechanical analysis with an ALE formulation was used. The ALE formulation is a suitable alternative to the classic Lagrangian formulation for mesh size control, which is inevitable due to the large deformation [34]. The friction between surfaces was defined using the Coulomb friction model, and the friction coefficient was selected according to Table 3. Surface-to-surface contact with a penalty formulation has been confirmed suitable for the model. In the flow-forming process, the material deformation is high, and the contact conditions are complex. Therefore, because of the numerical resilience and computing efficiency in highly nonlinear and large-scale applications, a dynamic-explicit solution approach was utilized in this simulation [35]. In addition, to speed up the calculation, the mass scaling factor was applied. The parameters used in this simulation are shown in Table 4.

## Results

### Simulation and Experiment

The findings of simulations and experiments are discussed in this section. The gear teeth were created gradually in four steps during the production process. After a 25% thickness reduction, the first preform was removed from the mandrel. After reducing the thickness in the first step (25%), the second step also reduced the thickness by 25% and removed the mandrel. The third preform after a 25% reduction in thickness (in step-1 and step-2) was reduced by 20% in the third step. The fourth preform after three steps of thickness reduction according to the third preform was reduced by 15% in the fourth step. The final product of the gear is shown in Fig. 7. To check the teeth' form, the parts (in each step)

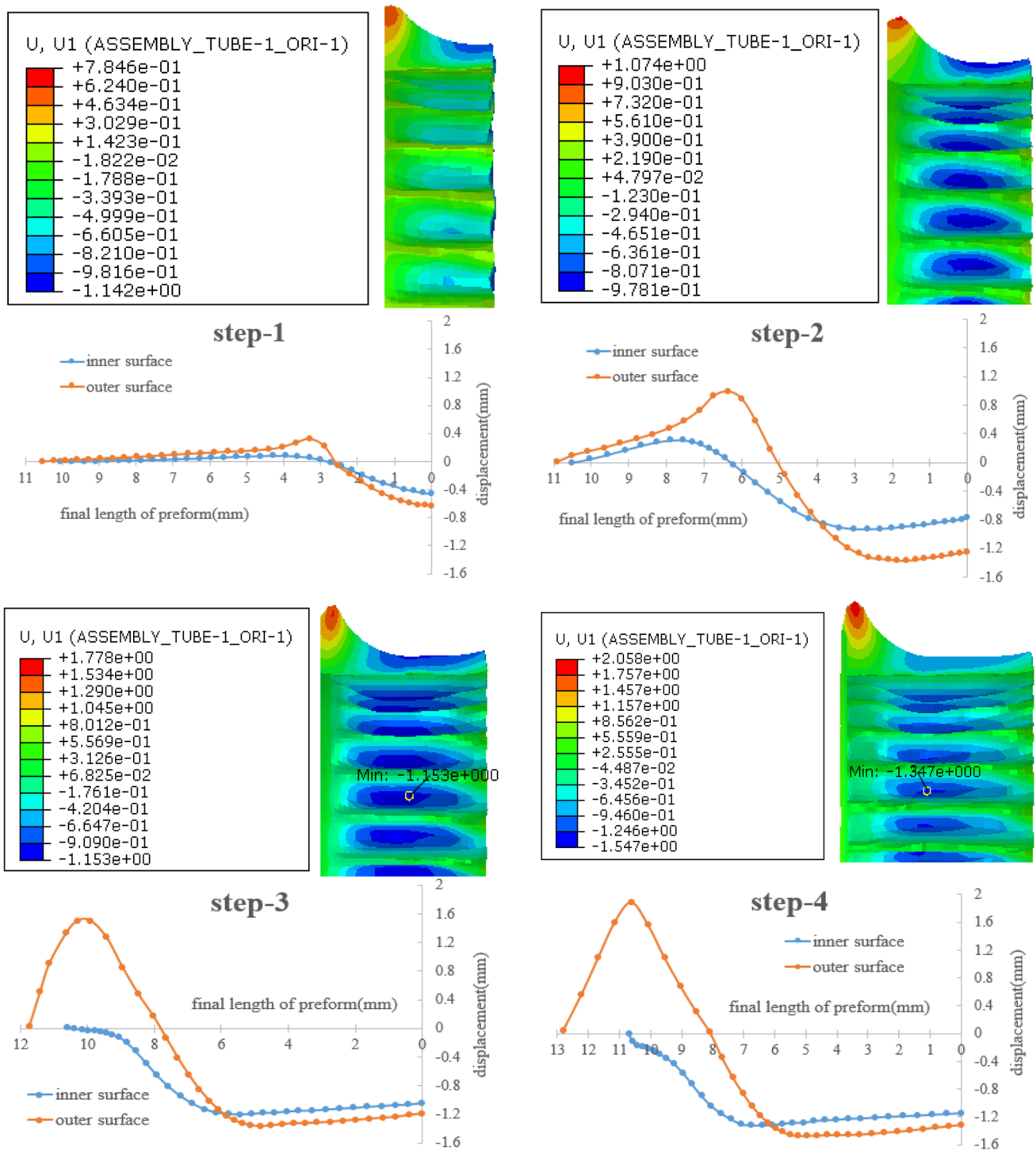


Fig. 9 Displacement of material in the outer and inner surface of internal gear (simulation)

were cut by EDM. Then, the cut parts were examined by the VMM machine, and their tooth form and height were evaluated. Figure 8 presents the form and height of a gear tooth in four steps, as determined by modeling and experimentation.

The process was also simulated in four steps. Figure 9 shows how the preform is deformed in the simulation.

The initial length of the preform in the simulation was considered to be 10 mm. As the roller advances on the preform, the material moves in axial and radial directions, increasing the length of the preform and forming teeth. The displacements of the inner and outer surfaces of the preform are shown in Fig. 9. The inner surface of

the preform moves to fill the mandrel grooves and form teeth, and the outer surface of the preform moves outward, causing the material to accumulate in front of the roller and form the built-up edge. The accumulation of material in front of the roller causes the material to move slightly away from the mandrel due to its movement and increases the inner diameter, which is quite evident in the first and second steps (blue diagram). However, in the third and fourth steps, as the roller moves, this defect disappears. As can be seen, the displacement of the inner surface under the roller is larger than the displacement of the outer surface because some of the thickness reduction leads to an increase in length. The tooth height and the built-up edge are small in the first step and gradually increase in the later steps. In Fig. 10 and Table 5, the height and form of the teeth are compared in both experimental and simulation modes, and it is observed that the results of experiments and simulations are in good accord.

### Microstructure of Gear

In this process, the workpiece turns into gear in four steps of cold plastic deformation, and due to mechanical work, the microstructure of the workpiece changes. The microstructure of flow-formed gear can be studied to understand the deformation mechanism better. To analyze the microstructure, samples from the preform and various gear sections were prepared. The specimens were immersed in a solution consisting of 19% HCl, 3% FeCl<sub>3</sub>, and 76% C<sub>2</sub>H<sub>5</sub>OH (volume fraction). Finally, a light microscope was used to examine the samples' microstructures. Microstructures of the original preform and gear were obtained (Fig. 11). As shown in Fig. 11(a), the microstructure of the preform consists of equiaxed grains. However, as Fig. 11(b) shows, the orientation of

the grains is in the radial and tangential directions and aligned with the filling of the mandrel grooves. Some samples were also prepared from two sections, A and B, of the gear (Fig. 12). The microstructures of these two sections are shown in Fig. 13.

As can be seen, the grains of section B are more irregular and elongated than those of section A because the material is compressed and deformed more between the roller and the mandrel teeth. In section A, the material enters the mandrel groove in the first step and forms part of the tooth, but in the latter step, this part of the tooth, due to the pressure of adjacent regions, enters the mandrel groove more and has less deformation than part B. Therefore, the microstructural changes of this part are less, which is consistent with the results of the reference [20].

A microhardness test was also performed on sections A and B (from the outer surface to the inner surface). In a Vickers hardness (HV) measurement, the amount of force is 100 grams, and the settling time is 10 seconds. The hardness measured in sections A and B is shown in Fig. 14. In section A (Fig. 14(a)), from the exterior to the inner surface, the hardness diminishes. The peripheral part of the gear is formed under the roller and by its pressure, and the grains are pulled in the roller's direction. On the other hand, as mentioned, the microstructure of the tip of section A does not change much, so the hardness decreases from the external environment to the tip of the tooth. In section B (Fig. 14(b)), the length of the graphs also varies according to the different thicknesses in each step. In steps 1 and 2, the hardness changes are similar to those in section A, and the hardness increases from the inside to the outside. However, in steps 3 and 4, due to the small thickness, the grain deformation is almost equal, and the hardness of this section does not change much. Because the deformation is high in steps 3 and 4, the hardness is higher than in the first and second steps.

### Effect of Parameters on the Process Temperature

One of the critical variables in the flow-forming process is the process temperature. Temperature represents both the process execution and the friction, and affects the mechanical properties of the workpiece and the tool life.

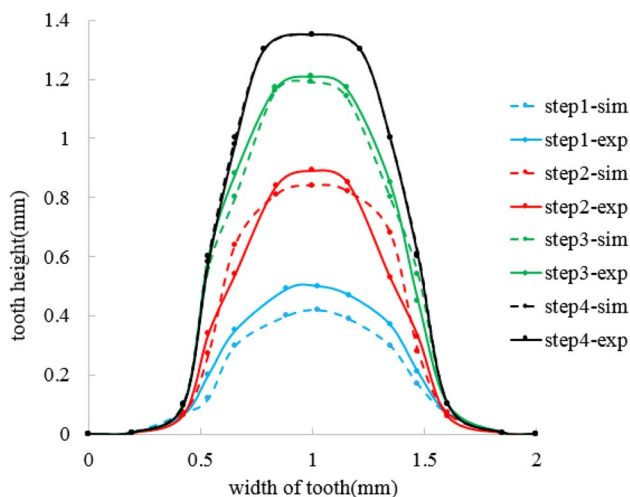
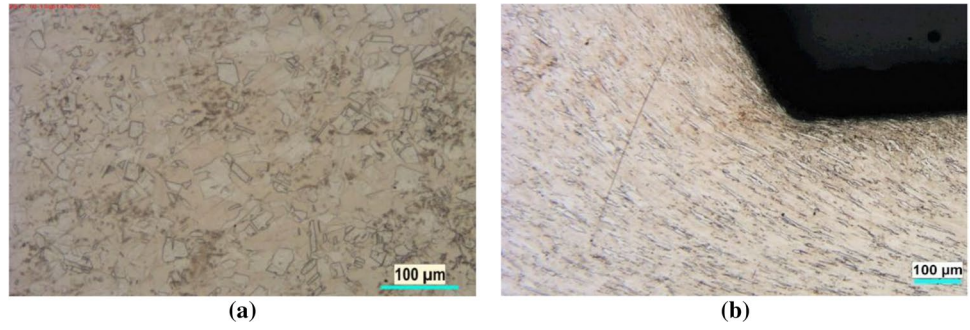


Fig. 10 Tooth height in the experiment and simulation

Table 5 Comparison of tooth height in the experiment and simulation

	Step-1	Step-2	Step-3	Step-4
Simulation	0.44	0.84	1.19	1.35
experiment	0.5	0.89	1.21	1.35
% error	12%	5%	2%	0

**Fig. 11** Microstructure of (a) preform (equiaxed grains), (b) flow-formed gear (elongated grains)



Therefore, the temperature must be carefully controlled during the process to achieve the desired mechanical properties and prevent premature failure of the tool. In metal forming processes, the process temperature depends on four factors: the initial temperature of the workpiece and the tool; the heat from the friction between the workpiece and the tool; the heat production due to the plastic deformation; and the heat transmission between the workpiece and the tool and the environment. The average temperature of the workpiece can be shown in equation (3).

$$T_m = T_d + T_f + T_t \quad (3)$$

$$T_d = \frac{\beta}{\rho C} \int \sigma d\epsilon \quad (4)$$

$T_d$  is the temperature due to plastic deformation (equation (4)),  $T_f$  is the temperature due to friction, and  $T_t$  is the temperature exchanged with the environment. In equation (3),  $\beta$  is the part of the deformation energy converted to heat (95%),  $\rho$  is the density, and  $C$  is the specific heat of the workpiece. According to equation (3), the higher the stress required for the deformation, the higher the deformation energy and process temperature. On the other hand, this process can be considered similar to the extrusion process [36], and therefore the deformation energy can be regarded as equation (5).

$$U_T = U_p + U_f + U_r \quad (5)$$

$U_p$  is the work of plastic deformation,  $U_f$  is the work of friction, and  $U_r$  is the extra work that exists in the internal

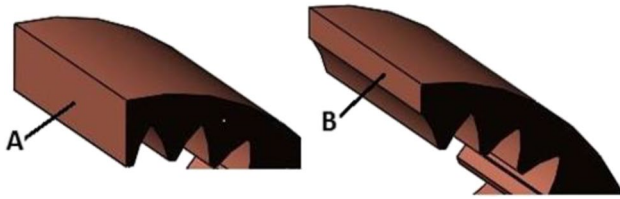


**Fig. 12** Various sections of internal gear selected for metallography

**Fig. 13** Sections of the gear whose microstructure is examined

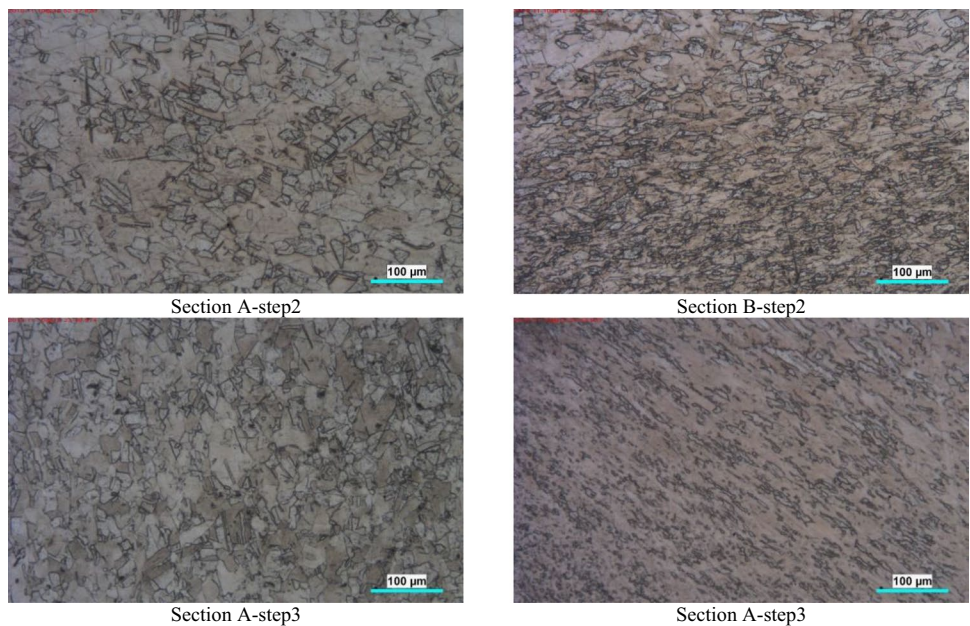
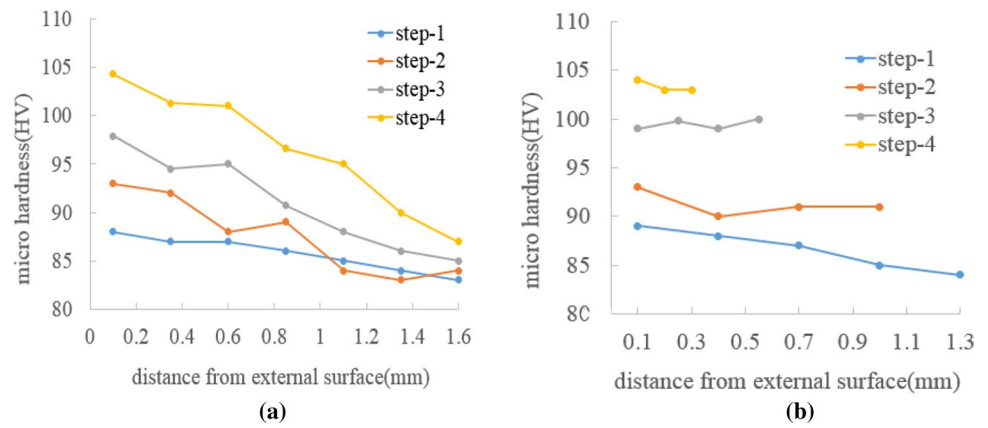


**Fig. 14** Measured microhardness for (a) section A and (b) section B



shear process due to non-uniform deformation and does not interfere with the deformation of the body. By increasing the die angle in the extrusion (the attack angle of contact of the roller with the preform in the flow-forming), the amount of redundant work increases [37, 38].

In this paper, the response surface method (RSM) was utilized to study the parameters affecting the process temperature. Feed rate, roller diameter, attack angle of the roller, and thickness reduction percentage (as shown in Fig. 15) are more important parameters than others in flow-forming [35], and their levels are given in Table 6.

The results of the analysis of variance (ANOVA) for process temperature, after eliminating the ineffective parameters ( $D \times \alpha$  and  $T \times T$ ) are shown in Table 7. When estimating a parameter, the degree of freedom (DF) refers to the number of observations or data points that can have different values without any restrictions. The total corrected sum of squares (SS) is used to measure the overall variability in the data. The mean of squares (MS) is calculated by dividing the (SS) by the (DF). The (F-value) is calculated by dividing the (MS) by the ( $MS_{error}$ ). In a hypothesis test, the probability value (p-value) is equal to the minimum value of the significance level or the probability of the first type of error, which rejects the null hypothesis [39]. According to

the Pareto chart (Fig. 16(a)) and the last column of Table 7, the parameters of thickness reduction (T) and roller diameter (D) have the most significant effect on process temperature. The regression equation for predicting process temperature is given in equation (6).  $R^2 = 99.74$  and  $R^2_{adj} = 99.56$ , which confirm the high accuracy of predicting the temperature regression model, which was developed using the RSM. The residuals in Fig. 16(b) also have a suitable normal distribution.

$$T(^{\circ}C) = -39.70 - 0.970 D + 3.685 T + 232.3 f + 2.642 \alpha + 0.01028 D * D - 1188.8 f * f - 0.01972 \alpha * \alpha - 0.01187 D * T + 1.313 D * f + 4.125 T * f - 0.02813 T * \alpha - 1.313 f * \alpha \quad (6)$$

The main effects and interaction plots of parameters on process temperature are shown in Figs. 17 and 18, respectively. The process temperature decreases as the roller diameter increases. By increasing the roller diameter (to reduce the same thickness), the angle of contact of the roller with the preform and the excess work is reduced, less energy is required for deformation, and less heat is generated during the process. As the thickness reduction percentage is increased, the process temperature also increases. Because the plastic deformation area increases, and as a result, the deformation energy increases, which leads to a rise in temperature. On the other hand, as the thickness increases, the friction between the roller and the workpiece increases. Increasing the feed rate, increasing the process temperature, and after 0.15 mm/rev, it has a downward trend. As the feed rate increases, the deformation rate, and strain rate increase, so the stress required for the deformation increases. According to equation (3), as the stress increases, the temperature of the workpiece also increases. Also, with an increasing

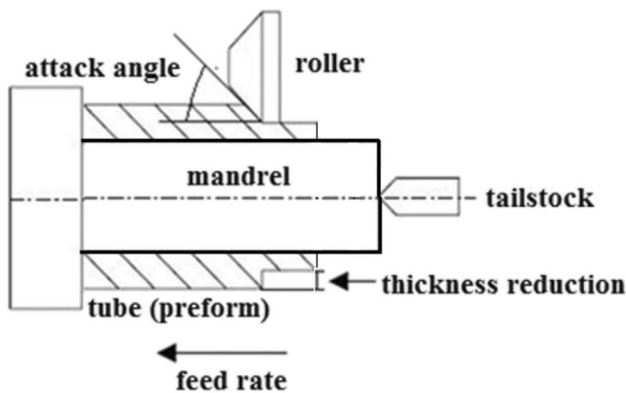


**Fig. 15** Schematic of effective parameters in the backward flow-forming process

**Table 6** The levels of effective parameters in IGFP

parameter	Feed rate(f)	Roller diameter(D)	Attack angle( $\alpha$ )	Thickness reduction (T %)
Minimum	0.05 mm/rev	20 mm	20 $^{\circ}$	15%
Maximum	0.25 mm/rev	60 mm	60 $^{\circ}$	35%



**Table 7** ANOVA results for process temperature

Source	DF	Adj SS	Adj MS	F-Value	P-Value	Contribution
Model	12	5096.52	424.71	571.40	0.000	99.74%
Linear	4	4627.13	1156.78	1556.33	0.000	90.55%
D	1	147.51	147.51	198.46	0.000	2.89%
T	1	4387.51	4387.51	5902.95	0.000	85.86%
f	1	27.09	27.09	36.45	0.000	0.53%
$\alpha$	1	65.01	65.01	87.46	0.000	1.27%
Square	3	401.32	133.77	179.98	0.000	7.85%
D*D	1	30.57	30.57	41.13	0.000	1.23%
f*f	1	255.46	255.46	343.70	0.000	4.42%
$\alpha*\alpha$	1	112.47	112.47	151.32	0.000	2.20%
2-Way Interaction	5	68.08	13.62	18.32	0.000	1.33%
D*T	1	5.64	5.64	7.59	0.013	0.11%
D*f	1	6.89	6.89	9.27	0.007	0.13%
T*f	1	17.02	17.02	22.89	0.000	0.33%
T* $\alpha$	1	31.64	31.64	42.57	0.000	0.62%
f* $\alpha$	1	6.89	6.89	9.27	0.007	0.13%
Error	18	13.38	0.74			0.26%
Lack-of-Fit	12	9.25	0.77	1.12	0.470	0.18%
Pure Error	6	4.13	0.69			0.08%
Total	30	5109.90				100.00%

strain rate, the temperature exchange of the workpiece with the environment decreases, and the temperature of the workpiece increases. This increase in temperature causes thermal softening of the workpiece and a reduction of deformation

stress. Therefore, with an increased feed rate from a specific limit, the process temperature decreases. By increasing the attack angle, the temperature increases and gradually decreases after 40°. By increasing the attack angle,

**Fig. 16** (a) Pareto chart, and (b) Normal probability of residuals for process temperature

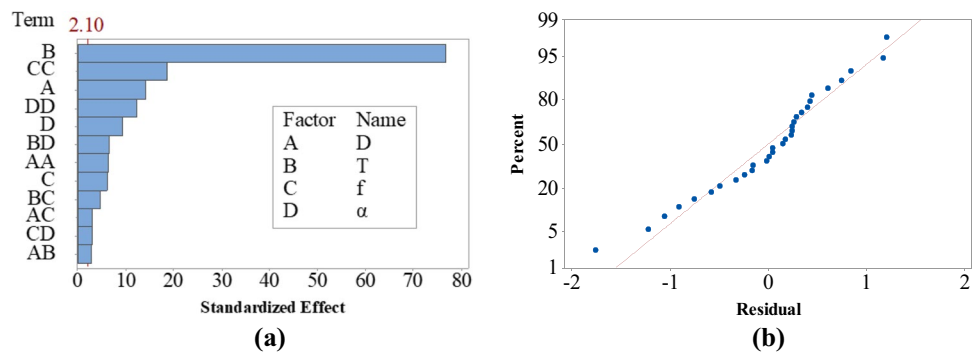


**Fig. 17** The main effects of parameters on process temperature

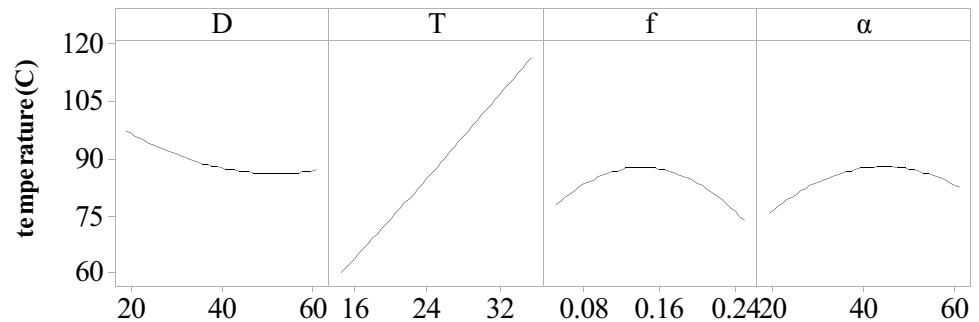
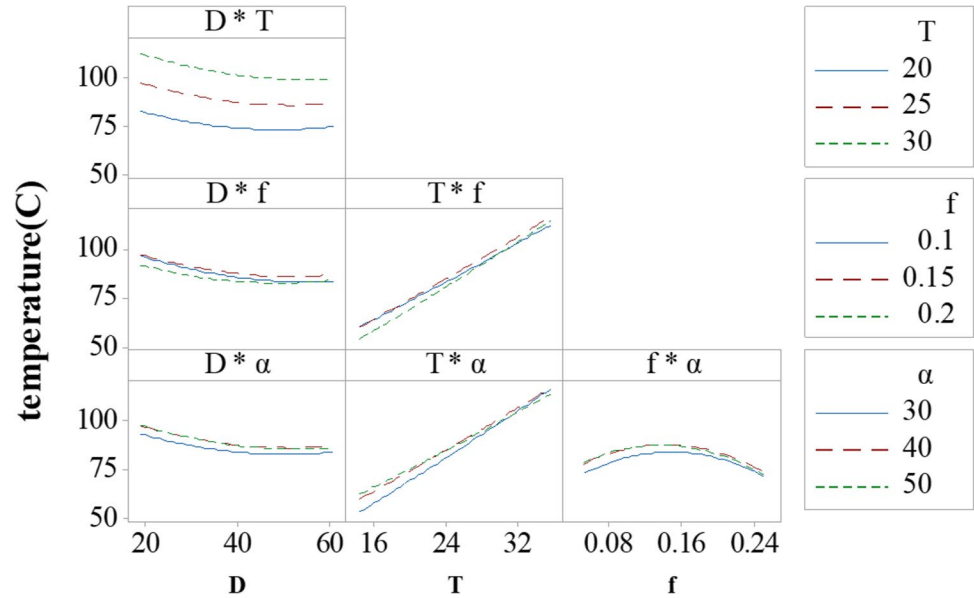


**Fig. 18** Interaction effects of parameters on process temperature



the amount of extra work to deform and, consequently, the deformation energy increase, which leads to the rise in temperature.

### Response Optimization

Since all engineering problems, besides being nonlinear, have many limitations, it is recommended to use meta-heuristic algorithms to find optimal solutions to these problems. Modern meta-heuristic algorithms have been constructed based on collective intelligence and nature-inspired.

The firefly algorithm is a meta-heuristic algorithm based on the behavior of light-generating fireflies. Fireflies can use chemical pathways to release stored energy obtained from food or other sources in the form of light. The firefly's aim in generating light is to absorb other fireflies in the group, attract prey, and reject obnoxious individuals. Three crucial assumptions must be taken into account when using this algorithm:

- Each firefly's attractiveness is proportional to its brightness, and all fireflies are of the same sex. If a firefly emits more light, it is more attractive than other fireflies and attracts fireflies from a shorter distance with less light.
- The brightness of the firefly diminishes as the distance between them grows.
- The brightness of each firefly represents a view of the problem's objective function.

The movement of a firefly towards a brighter firefly corresponds to the objective function's movement towards a better solution and, eventually, the optimal solution. When compared to genetic algorithms (GA) and particle swarm optimization (PSO), this algorithm is more efficient in finding general optimal spots and has a faster speed [40]. Other

researchers have successfully applied this approach in various technical domains, confirming its efficacy [41–44].

The attractiveness of a firefly is defined by the light intensity and brightness derived from the objective function. For the maximum optimization problems, the light intensity  $I$  of a firefly in a specific area  $\mathbf{X}$  can be defined as  $I(x) \propto f(x)$ . The light intensity of each firefly can be modeled according to equation (7).

$$I(r) = \frac{I_s}{r^2} \quad (7)$$

That  $I_s$  is the light intensity of the source. To avoid the singularity of  $r=0$  in (equation (7)), combining the effects of both inverse square and absorption laws approximates this relation to the Gaussian form (equation (7)). As a result, for an environment with a constant light absorption coefficient ( $\gamma$ ), the brightness  $I$  changes with distance  $r$  according to (equation (8)).

$$I = I_0 e^{-\gamma r} \quad (8)$$

By merging both equations (1) and (2), the final equation (equation (9)) must be used to calculate the brightness.

$$I(r) = I_0 e^{-\gamma r^2} \quad (9)$$

If we expand the above relation through the Taylor expansion, we will have equation (10):

$$I(r) = \frac{I_0}{1 + \gamma r^2} \quad (10)$$

The amount of attractiveness of a firefly is proportional to the light intensity seen by adjacent fireflies, so light intensity relationships also apply to attractiveness. However, the

attractiveness of  $\beta$  is relative because it must be seen in the eyes of the viewer by other fireflies. Therefore, attractiveness will change with the distance  $r_{ij}$  between the fireflies  $i$  and  $j$ . In addition, the reduction in light intensity is proportional to the distance from the source. Since the attractiveness of a firefly is proportional to the intensity of light seen by its adjacent firefly, the attractiveness ( $\beta$ ) can be defined as equation (11).

$$\beta = \beta_0 e^{-\gamma r^2} \quad (11)$$

Where  $\beta_0$  is attractiveness at  $r=0$ . In the actual implementation, the attractiveness function  $\beta(r)$  can be any uniformly decreasing function, such as the general formula in equation (12).

$$B(r) = \frac{\beta_0}{1 + \gamma r^m}, m \geq 1 \quad (12)$$

The greater the distance between the two fireflies, the less attractive it becomes. According to equation (13), it can be concluded that fireflies move towards fireflies that are closer. So two factors have priority: betterment and proximity.

$$X' = X + \beta(Y - X) \quad (13)$$

The distance property is defined according to equation (14).

$$\Gamma = 1/\sqrt{\gamma} \quad (14)$$

That the attractiveness changes significantly from  $\beta_0$  to  $\beta_0 e^{-1}$ . For a constant  $\gamma$ , the distance property can be defined as equation (15).

$$\Gamma = \gamma^{-\frac{1}{m}} \xrightarrow{m \rightarrow \infty} \Gamma \rightarrow 1 \quad (15)$$

The distance between the two fireflies  $i$  and  $j$  at  $x_i$  and  $x_j$  is the Cartesian distance given in equation (16).

$$r_{ij} = \|x_i - x_j\| = \sqrt{\sum_{k=1}^d (x_{i,k} - x_{j,k})^2} \quad (16)$$

Where  $x_{(i,k)}$ , is the  $k$  component of the coordinate distance  $x_i$  of the  $i$ -th firefly. Therefore, we will have equation (17).

$$r_{ij} = \sqrt{(x_i - x_j)^2 + (y_i - y_j)^2} \quad (17)$$

The displacement of a firefly  $i$  toward a more attractive (brighter) firefly  $j$  is defined as equation (18).

$$x_i = x_i + \beta_0 e^{-\gamma r_{ij}^2} (x_j - x_i) + \alpha \epsilon_i \quad (18)$$

Where the second term is related to attractiveness, the third term is the random maker parameter  $\alpha$ , and  $\epsilon_i$  is the random vector of the numbers shown from a Gaussian distribution

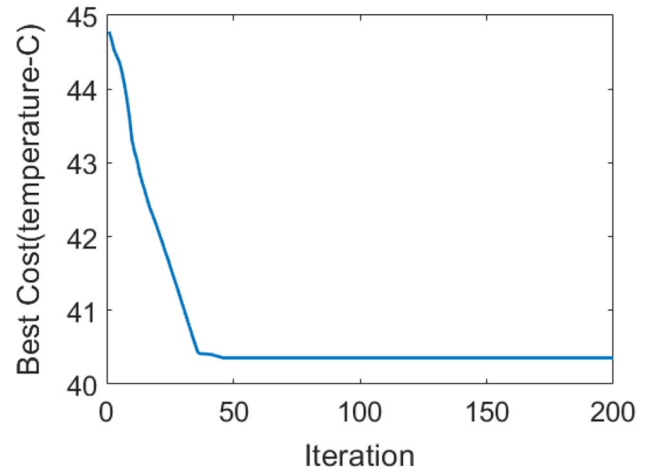


Fig. 19 Single objective FA algorithm iterations for process temperature

or a uniform distribution. For example, the simplest form is  $\epsilon_i$  and can be replaced by  $\text{rand}(-1/2)$ , where the  $\text{rand}$  is a uniform distribution that produces a random number in the range  $[0, 1]$ . For most implementations, we can consider  $\beta_0 = 1$  and  $\alpha \in [0, 1]$ . In this formula, the  $\gamma$  parameter specifies the types of attractiveness, and its value determines the convergence speed and how the firefly algorithm behaves. In theory,  $\gamma \in [0, \infty]$ , but in practice,  $\gamma = O(1)$  obtained by the distance property of  $\Gamma$ ; so in many programs, it usually varies from 0.1 to 10.

If  $\gamma \rightarrow 0$ , the attractiveness is constant  $\beta = \beta_0$  and  $\Gamma \rightarrow \infty$ . This formula states that the intensity of light in the ideal sky will not decrease; Thus, a flashing firefly can be seen anywhere in a specific range. Thus, a single optimal point can be easily achieved, but if the inner ring  $j$  is removed and  $x_j$  is chosen as the best worm without comparing its attractiveness with other worms, the firefly algorithm becomes a particular case of particle swarm optimization (PSO). The performance of this particular case is similar to that of PSO. On the other hand, if  $\gamma \rightarrow \infty$ ,  $\Gamma \rightarrow 0$ ,  $\beta(r) \rightarrow \delta(r)$ , which is a Dirac delta function. This means that the attractiveness of other fireflies is almost zero. This formula is for cases where fireflies accidentally roam in an area with thick fog. No other fireflies can be seen, and each firefly roams in an entirely random way; Therefore, this is a completely random search method. So  $\gamma$  partly controls how the algorithm behaves. It is also possible to adjust so that multiple optima can be found simultaneously during iterations [44, 45].

Table 8 Optimum design of input parameters for process temperature in FA algorithm

D (mm)	T (%)	f (mm/rev)	$\alpha$ (degree)	optimum value of temperature( $^{\circ}$ C)
20	15	0.25	60	40.36

**Table 9** Comparison between simulation results and optimization values

D(mm)	T(%)	f(mm/rev)	$\alpha$ (degree)	Process temperature (FA)	Process temperature (simulation)	error
20	15	0.25	60	40.36	43.12	7%

The following steps should be repeated until the stopping requirements are met, and the final optimal solution is reached when utilizing the firefly technique to solve the issues optimally:

1. The first stage is to generate a random population of fireflies. It is preferable to select all primary fireflies consistently throughout the allowable range in this phase.
2. For each firefly, calculate the value of the objective function and choose the best response.
3. Determine the attractiveness of the two fireflies and their distance.
4. Compare the value of each firefly's objective function to that of other fireflies.
5. Change the firefly to the most gorgeous (best) firefly.
6. To determine the fireflies' new position,
7. Return to step 2 if the stopping criteria are not met.

If the stopping criteria are met in step 7, the problem is solved optimally, and the best firefly location in the previous iteration is the most appropriate solution.

The results of FA optimization for process temperature are given in Fig. 19 and Table 8. Figure 19 shows the convergence of the optimization algorithm for process temperature. After about 200 iterations, the convergence condition is satisfied, and the minimum temperature converges to 40.36 °C. In Table 9, the optimization and

```

Objective function  $f(x)$ ,  $x = (x_1, \dots, x_d)^T$ 
Initialize a population of fireflies  $x_i$  ( $i = 1, 2, \dots, n$ )
Define light absorption coefficient
while ( $t < \text{MaxGeneration}$ )
for  $i = 1 : n$  all  $n$  fireflies
  for  $j = 1 : i$  all  $n$  fireflies
    Light intensity  $I_j$  at  $x_j$  is determined by  $f(x_j)$ 
    if ( $I_j > I_i$ )
      Move firefly  $i$  towards  $j$  in all  $d$  dimensions
    end if
    Attractiveness varies with distance  $r$  via  $\exp[-\gamma r]$ 
    Evaluate new solutions and update light intensity
  end for  $j$ 
end for  $i$ 
Rank the fireflies and find the current best
end while
Post process results and visualization

```

Firefly Algorithm

simulation results are compared. A good agreement can be seen between these results.

## Conclusion

In the present study, the manufacturing of internal gears was investigated numerically and experimentally. First, Finite element software was used to simulate the process, and the possibility of manufacturing an internal gear was investigated. Then, by performing experiments, the simulation results were validated. Then the metallurgical properties of the preform and product were examined by light microscopy. Also, in this study, the effect of process parameters, including feed rate, roller diameter, attack angle of the roller, and thickness reduction percentage, on process temperature was investigated. This investigation was performed by the design of experiments (DOE) and the response surface method (RSM). In the end, this function was optimized, and the final optimal point for process temperature was determined. The results of this research are briefly mentioned in this section:

- The microstructure of the preform consists of equiaxed grains. However, the orientation of the grains in the final product is in the radial and tangential directions and aligned with the filling of the mandrel grooves.
- All parameters and their interactions, except  $D \times \alpha$  and  $T \times T$ , affect the process temperature. The parameters of thickness reduction (T) and roller diameter (D) have the most significant effect on the process temperature. The process temperature decreases as the roller diameter increases. As the thickness reduction decreases, the process temperature increases. The process temperature rises and then falls as the feed rate rises to 0.15 mm/rev. By increasing the attack angle to 40 degrees, the process temperature increases and then decreases.
- According to the FA algorithm results, the minimum temperature value was 40.36° C, related to  $D = 20$  mm,  $T = 15\%$ ,  $f = 0.25$  mm/rev, and  $\alpha = 60^\circ$ .

## Declarations

1. The study does not involve the sampling/participation of humans or animals in any aspect.
2. All authors made substantial contributions and contributed equally to the manuscript in all aspects.
3. The study was not funded by any funding organization.
4. The authors declare that there is no conflict of interest.
5. The datasets generated, and/or analyzed during the current study are available from the corresponding author on reasonable request.



## References

- Srinivasulu M, Komaraiah M, Krishna Prasada Rao CS (2013) Prediction of the surface roughness of AA6082 flow-formed tubes by design of experiments. *J Mech Sci Technol* 27(6):1835–1842. <https://doi.org/10.1007/s12206-013-0434-y>
- Bhatt RJ, Raval HK (2018) In situ investigations on forces and power consumption during flow forming process. *J Mech Sci Technol* 32(3):1307–1315. <https://doi.org/10.1007/s12206-018-0235-4>
- Gao PF, Li M, Zhan M, Xing L, Ma F, Fu MW (2021) Circumferential twist in flow forming of tubular parts: Characterization, understanding and control. *J Manuf Process* 65:144–152. <https://doi.org/10.1016/j.jmapro.2021.03.020>
- Podder B, Banerjee P, Kumar KR, Hui NB (2020) Forward and reverse modelling of flow forming of solution annealed H30 aluminium tubes. *Neural Comput Appl* 32(7):2081–2093. <https://doi.org/10.1007/s00521-018-3749-x>
- Shi N, Wang W-x, Zhang T-t, Chen H-s, Chen W, Feng R-y (2021) Interface bonding and deformation behavior of 6061Al/AZ31Mg composite tubes fabricated by stagger spinning. *Trans Indian Inst Met* 74(6):1373–1385. <https://doi.org/10.1007/s12666-020-02042-3>
- Srivastwa AK, Singh PK, Kumar S (2021) Experimental investigation of flow forming forces in Al7075 and Al2014 – A comparative study. *Mater Today: Proc* 47:2715–2719. <https://doi.org/10.1016/j.matpr.2021.02.781>
- Zhang J, Wang W, Zhang T, Yan Z, Shi N (2021) Mechanical characterization of the plastic deformation behavior of AZ31 magnesium alloy processed through spinning using nanoindentation. *Trans Indian Inst Met* 74(6):1349–1359. <https://doi.org/10.1007/s12666-021-02218-5>
- Rieppold M, Arian B, Roza Vasquez J, Homberg W, Walther F, Trächtler A (2021) Model approaches for closed-loop property control for flow forming. *Adv Ind Manuf Eng* 3:100057. <https://doi.org/10.1016/j.aime.2021.100057>
- Gao P, Yu C, Fu M, Xing L, Zhan M, Guo J (2021) Formability enhancement in hot spinning of titanium alloy thin-walled tube via prediction and control of ductile fracture. *Chin J Aeronaut*. <https://doi.org/10.1016/j.cja.2021.01.002>
- Cheng Y-C, Lin C-K, Tan A-H, Hsu S-Y, Lee S-L (2012) Effect of the spinning deformation processing on mechanical properties of Al-7Si-0.3Mg alloys. *J Mater Eng Perform* 21(9):1873–1878. <https://doi.org/10.1007/s11665-011-0089-8>
- Groche P, Fritsche D (2006) Application and modelling of flow forming manufacturing processes for internally geared wheels. *Int J Mach Tools Manuf* 46(11):1261–1265
- Khodadadi M, Khalili K, Ashrafi A (2020) Studying the effective parameters on teeth height in internal gear flowforming process. *Int J Eng* 33(12):2563–2571. <https://doi.org/10.5829/ije.2020.33.12c.18>
- Khodadadi M, Khalili K, Ashrafi A (2021) Study on manufacturing of internal gear by flowforming process and investigation of effective parameters on process force. *Iran J Mater Form* 8(1):14–25. <https://doi.org/10.22099/ijmf.2020.37889.1162>
- Khodadadi M, Khalili K, Ashrafi A (2022) Optimizing parameters effective on built-up edge in internal gear flow-forming process. *Sādhanā* 47(2):99. <https://doi.org/10.1007/s12046-022-01860-z>
- Nägele H, Wörner H, Hirschvogel M (2000) Automotive parts produced by optimizing the process flow forming – machining. *J Mater Process Technol* 98(2):171–175. [https://doi.org/10.1016/S0924-0136\(99\)00195-8](https://doi.org/10.1016/S0924-0136(99)00195-8)
- Guba N, Hüsemann T, Karpuschewski B (2020) Influence of gear hobbing feed marks on the resulting gear quality after discontinuous profile grinding. *CIRP J Manuf Sci Technol*. <https://doi.org/10.1016/j.cirpj.2020.06.005>
- Jiang S-Y, Ren Z-Y, Bin W, Wu G-X (2007) General issues of FEM in backward ball spinning of thin-walled tubular part with longitudinal inner ribs. *Trans Nonferrous Met Soc China* 17(4):793–798
- Jiang S, Ren Z, Xue K, Li C (2008) Application of BPANN for prediction of backward ball spinning of thin-walled tubular part with longitudinal inner ribs. *J Mater Process Technol* 196(1–3):190–196
- Jiang S, Ren Z, Li C, Xue K (2009) Role of ball size in backward ball spinning of thin-walled tubular part with longitudinal inner ribs. *J Mater Process Technol* 209(4):2167–2174
- Jiang S-Y, Zheng Y-F, Ren Z-Y, Li C-F (2009) Multi-pass spinning of thin-walled tubular part with longitudinal inner ribs. *Trans Nonferrous Met Soc China* 19(1):215–221
- Haghshenas M, Jhaver M, Klassen R, Wood J (2011) Plastic strain distribution during splined-mandrel flow forming. *Mater Design* 32(6):3629–3636
- Haghshenas M, Wood J, Klassen R (2012) Investigation of strain-hardening rate on splined mandrel flow forming of 5052 and 6061 aluminum alloys. *Mater Sci Engineering: A* 532:287–294
- Haghshenas M, Wood J, Klassen R (2012) Effect of strain-hardening rate on the grain-to-grain variability of local plastic strain in spin-formed fcc metals. *Mater Sci Eng: A* 552:376–383
- Xia Q-X, Sun L-Y, Cheng X-q, Ye B-Y (2009) Analysis of the forming defects of the trapezoidal inner-gear spinning. In: *Industrial Engineering and Engineering Management, IEEM 2009. IEEE International Conference on, 2009. IEEE*, pp 2333–2337
- Xia Q, Long J, Xiao G, Yuan S, Qin Y (2021) Deformation mechanism of ZK61 magnesium alloy cylindrical parts with longitudinal inner ribs during hot backward flow forming. *J Mater Process Technol* 296:117197. <https://doi.org/10.1016/j.jmatprotec.2021.117197>
- Xu W, Zhao X, Shan D, Li J, Deng Q, Cui X, Li Z (2016) Numerical simulation and experimental study on multi-pass stagger spinning of internally toothed gear using plate blank. *J Mater Process Technol* 229:450–466
- Ong P, Chin DDVS, Ho CS, Ng CH (2018) Modeling and optimization of cold extrusion process by using response surface methodology and metaheuristic approaches. *Neural Comput Appl* 29(11):1077–1087. <https://doi.org/10.1007/s00521-016-2626-8>
- Zieter G (1986) *Mechanical metallurgy*. McGraw-Hill, Singapore
- Zhu Y, Zeng W, Ma X, Tai Q, Li Z, Li X (2011) Determination of the friction factor of Ti-6Al-4V titanium alloy in hot forging by means of ring-compression test using FEM. *Tribol Int* 44(12):2074–2080. <https://doi.org/10.1016/j.triboint.2011.07.001>
- Martín F, Martín MJ, Sevilla L, Sebastián MA (2015) The ring compression test: Analysis of dimensions and canonical geometry. *Procedia Eng* 132:326–333. <https://doi.org/10.1016/j.proeng.2015.12.502>
- Moncada A, Martín F, Sevilla L, Camacho AM, Sebastián MA (2015) Analysis of ring compression test by upper bound theorem as special case of non-symmetric part. *Procedia Eng* 132:334–341. <https://doi.org/10.1016/j.proeng.2015.12.503>
- Cristino VAM, Rosa PAR, Martins PAF (2015) The role of interfaces in the evaluation of friction by ring compression testing. *Exp Tech* 39(4):47–56. <https://doi.org/10.1111/j.1747-1567.2012.00857.x>
- Rasouli MA, Taherizadeh A, Farzin M, Abdolah A, Niroomand MR (2017) Investigating the effects of process parameters on forming forces and defects formation in tube spinning process of AA6061. *Modares Mech Eng* 16(12):186–194

34. Crutzen Y, Boman R, Papeleux L, Ponthot J-P (2018) Continuous roll forming including in-line welding and post-cut within an ALE formalism. *Finite Elem Anal Des* 143:11–31. <https://doi.org/10.1016/j.finel.2018.01.005>
35. Wong C, Dean T, Lin J (2004) Incremental forming of solid cylindrical components using flow forming principles. *J Mater Process Technol* 153:60–66
36. Wong CC, Dean TA, Lin J (2003) A review of spinning, shear forming and flow forming processes. *Int J Mach Tools Manuf* 43(14):1419–1435. [https://doi.org/10.1016/S0890-6955\(03\)00172-X](https://doi.org/10.1016/S0890-6955(03)00172-X)
37. Gur M, Tirosch J (1982) Plastic flow instability under compressive loading during shear spinning process. *J Eng Ind* 104(1):17–22. <https://doi.org/10.1115/1.3185791>
38. Dieter GE (1988) *Mechanical metallurgy*, vol 1. Mc Graw-Hill, New York
39. Montgomery DC (2017) *Design and analysis of experiments*. Wiley, Hoboken
40. Yang X-S (2010) Firefly algorithm, stochastic test functions and design optimisation. *Int J Bio-Inspired Comput* 2(2):78–84. <https://doi.org/10.1504/ijbic.2010.032124>
41. Apostolopoulos T, Vlachos A (2011) Application of the Firefly Algorithm for solving the economic emissions load dispatch problem. *Int J Combinatorics* 2011:523806. <https://doi.org/10.1155/2011/523806>
42. Zang H, Zhang S, Hapeshi K (2010) A review of nature-inspired algorithms. *J Bionic Eng* 7:S232–S237. [https://doi.org/10.1016/S1672-6529\(09\)60240-7](https://doi.org/10.1016/S1672-6529(09)60240-7)
43. Coelho LdS, Mariani VC (2012) Firefly algorithm approach based on chaotic Tinkerbell map applied to multivariable PID controller tuning. *Comput Math Appl* 64(8):2371–2382. <https://doi.org/10.1016/j.camwa.2012.05.007>
44. Sababha M, Zohdy M, Kafafy M (2018) The enhanced firefly algorithm based on modified exploitation and exploration mechanism. *Electronics* 7(8):132
45. Bharathi RS, Srinivas Pramod CV, Vamshee Krishna K, Raguathan A, Vinesh S (2015) Optimization of electrical discharge machining parameters on hardened die steel using Firefly Algorithm. *Eng Comput* 31(1):1–9. <https://doi.org/10.1007/s00366-013-0320-3>

**Publisher's Note** Springer Nature remains neutral with regard to jurisdictional claims in published maps and institutional affiliations.

Springer Nature or its licensor (e.g. a society or other partner) holds exclusive rights to this article under a publishing agreement with the author(s) or other rightsholder(s); author self-archiving of the accepted manuscript version of this article is solely governed by the terms of such publishing agreement and applicable law.